Front. Chem. Sci. Eng. 2020, 14(6): 997–1005
https://doi.org/10.1007/s11705-019-1906-0

RESEARCH ARTICLE

Ultrathin microcrystalline hydrogenated Si/Ge alloyed tandem solar cells towards full solar spectrum conversion

Yu Cao[1,2], Xinyun Zhu[1,2], Xingyu Tong[1,2], Jing Zhou (✉)[3], Jian Ni[4], Jianjun Zhang[4], Jinbo Pang (✉)[5]

1 Key Laboratory of Modern Power System Simulation and Control & Renewable Energy Technology, Northeast Electric Power University, Jilin 132012, China
2 School of Electrical Engineering, Northeast Electric Power University, Jilin 132012, China
3 School of Chemical Engineering, Northeast Electric Power University, Jilin 132012, China
4 Key Laboratory of Photo-electronics Thin Film Devices and Technique of Tianjin, Institute of Photo-electronic Thin Film Devices and Technology, College of Electronic Information and Optical Engineering, Nankai University, Tianjin 300350, China
5 Collaborative Innovation Center of Technology and Equipment for Biological Diagnosis and Therapy in Universities of Shandong, Institute for Advanced Interdisciplinary Research (iAIR), University of Jinan, Jinan 250022, China

Abstract Thin film solar cells have been proved the next generation photovoltaic devices due to their low cost, less material consumption and easy mass production. Among them, micro-crystalline Si and Ge based thin film solar cells have advantages of high efficiency and ultrathin absorber layers. Yet individual junction devices are limited in photoelectric conversion efficiency because of the restricted solar spectrum range for its specific absorber. In this work, we designed and simulated a multi-junction solar cell with its four sub-cells selectively absorbing the full solar spectrum including the ultraviolet, green, red as well as near infrared range, respectively. By tuning the Ge content, the record efficiency of 24.80% has been realized with the typical quadruple junction structure of a-Si:H/a-$Si_{0.9}Ge_{0.1}$:H/μc-Si:H/μc-$Si_{0.5}Ge_{0.5}$:H. To further reduce the material cost, thickness dependent device performances have been conducted. It can be found that the design of total thickness of 4 μm is the optimal device design in balancing the thickness and the *PCE*. While the design of ultrathin quadruple junction device with total thickness of 2 μm is the optimized device design regarding cost and long-term stability with a little bit more reduction in *PCE*. These results indicated that our solar cells combine the advantages of low cost and high stability. Our work may provide a general guidance rule of utilizing the full solar spectrum for developing high efficiency and ultrathin multi-junction solar cells.

Received July 30, 2019; accepted October 9, 2019

E-mails: zhoujing@neepu.edu.cn (Zhou J); jinbo.pang@hotmail.com, ifc_pangjb@ujn.edu.cn (Pang J)

Keywords thin films, solar cells, quadruple junction solar cell, amorphous silicon, silicon germanium alloy, quantum efficiency

1 Introduction

Clean energy [1,2], especially solar energy harvesting remains of great interest for its infinite and clean energy nature [3−5]. Thin-film solar cells (TFSCs) have been receiving considerable attention for application in building integrated photovoltaic products due to their advantages, such as device flexibility and large module [6−11]. Over the last decade, the performance of the TFSCs has shown remarkable improvements owing to the development of the multi-junction TFSC structure [12−15]. The organic and perovskite TFSCs were successfully introduced into the tandem cell structure and shown encouraging results [16−19]. The Sb_2Se_3 and Sb_2S_3 TFSCs with similar microstructure and fabrication process also demonstrate their potential to combine as the multi-junction TFSC [20,21]. Furthermore, for silicon-based TFSCs, multi-junction structure can not only reduce thermalization and non-absorption losses by making the sub-cells with different band-gap absorb corresponding solar spectrum but also partly surpass the Staebler-Wronski effect by decreasing the thickness of the amorphous-based sub-cells. The hydrogenated amorphous silicon (a-Si:H)/hydrogenated microcrystalline silicon (μc-Si:H) tandem TFSCs have evolved into mainstream commercial products [22]. Moreover, an initial power conversion efficiency (*PCE*) of over 16% was achieved using an a-Si:H/hydrogenated amorphous silicon germanium (a-$Si_{1-x}Ge_x$:H)/μc-Si:H

triple junction TFSC structure by several research groups [23].

In recent years, novel quadruple junction TFSCs have been realized and some promising results have been observed [24]. Si et al. introduced hydrogenated amorphous silicon oxides (a-SiO_z:H) TFSC as the top sub-cell, and a *PCE* of 11.4% was obtained by using an a-SiO_z:H/a-Si:H/μc-Si:H/μc-Si:H cell structure [25]. Then, the a-Si:H/a-Si:H/μc-Si:H/μc-Si:H quadruple junction TFSC with an efficiency of 13.2% was achieved by Urbain et al. This TFSC was applied in an integrated photoelectrochemical water splitting device due to its high open voltage (V_{oc}) [26]. Furthermore, Liu et al. reported a high V_{oc} of over 3 eV and a *PCE* of 15.03% with an a-SiC_z:H/a-Si:H/a-$Si_{1-x}Ge_x$:H/μc-Si:H cell structure [24]. From these investigations, one can observe that no consensus has been reached on the optimal combination of the sub-cells, and the *PCE* of the quadruple junction still demonstrates a great upside potential.

The required spectral utilization efficiency for multi-junction TFSCs depends on the number of sub-cells. Normally, μc-Si:H TFSC is used as the third and fourth sub-cells in the quadruple junction TFSCs. However, a graded distribution of band-gaps could not be generated between these two sub-cells, as the band-gaps are unmodifiable. Furthermore, the infrared energy could not be used efficiently due to the weak absorption coefficient of the sub-cell. To overcome these drawbacks, hydrogenated microcrystalline silicon germanium (μc-$Si_{1-y}Ge_y$:H) has been developed as an alternative bottom sub-cell absorber for multi-junction TFSCs due to its narrow variable band-gap and high absorption coefficient [27]. In recent years, μc-$Si_{1-y}Ge_y$:H has been used in the tandem and triple junction TFSCs [28]. A *PCE* of 11.35% has been reported for the a-Si:H/a-$Si_{0.6}Ge_{0.4}$:H/μc-$Si_{0.5}Ge_{0.5}$:H triple junction structure with a total cell thickness as thin as 1200 nm [29]. This establishes the immense potential of this absorber to be employed as the bottom sub-cell absorber for the quadruple junction silicon-based TFSCs.

In this work, an a-Si:H/a-$Si_{1-x}Ge_x$:H/μc-Si:H/μc-$Si_{1-y}Ge_y$:H cell structure is proposed, and a theoretical study was performed to optimize the configuration of the quadruple junction TFSCs. Firstly, the most optimal combination of the Ge contents in a-$Si_{1-x}Ge_x$:H and μc-$Si_{1-y}Ge_y$:H sub-cells was determined to achieve the maximum *PCE* of the cell structure. Secondly, the optimal *PCE* of the quadruple junction TFSCs with varied thickness values was investigated. Finally, the performances of the quadruple junction TFSCs and triple junction TFSCs that employed μc-$Si_{1-y}Ge_y$:H as the bottom sub-cells were compared and analyzed.

2 Device simulation setup

The simulator adopted in this work is wxAMPS, which is an updated version of the Analysis of Microelectronic and Photonic Structure (AMPS) [30]. The simulator can calculate the solar cell parameters, carrier recombination profile, and electrical field distribution by solving the Poisson's equation (1) and continuity equations for electrons and holes (2, 3) [31], which are listed as follows:

$$\frac{\mathrm{d}}{\mathrm{d}x}\left(-\varepsilon(x)\frac{\mathrm{d}\phi}{\mathrm{d}x}\right) = q\left[p(x)-n(x)+p_{\mathrm{t}}(x)-n_{\mathrm{t}}(x)+N_{\mathrm{d}}^{+}(x)-N_{\mathrm{a}}^{-}(x)\right], \tag{1}$$

where the electrostatic potential ϕ, and the free holes p, free electrons n, trapped holes p_t and trapped electrons n_t, as well as the ionized donor-like doping $N_d^+(x)$ and ionized acceptor-like doping $N_a^-(x)$ concentrations are all functions of the position coordinate x. Here, q is the magnitude of the charge of an electron and ε is the permittivity.

$$\frac{\partial n(x,t)}{\partial t} = \frac{1}{q}\frac{\partial J_n}{\partial x} + G_n(x) - R_n(x), \tag{2}$$

$$\frac{\partial p(x,t)}{\partial t} = \frac{1}{q}\frac{\partial J_p}{\partial x} + G_p(x) - R_p(x), \tag{3}$$

where J_n, G_n and R_n are the density, the generation and recombination rate of electrons, and J_p, G_p besides R_p are the density, the generation and recombination rate of holes.

The structure of a quadruple junction TFSC (a-Si:H/a-$Si_{1-x}Ge_x$:H/μc-Si:H/μc-$Si_{1-y}Ge_y$:H) is shown in Fig. 1. The details of the model are given in S. 1 of the electronic supplementary material (ESM).

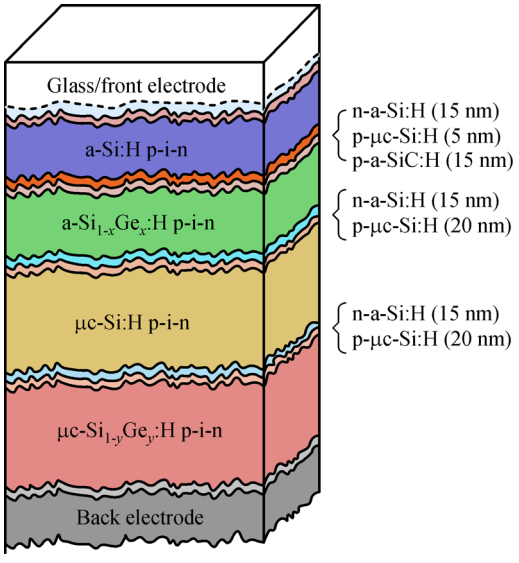

Fig. 1 Schematic of the silicon-based quadruple junction cell structure.

3 Results and discussion

The most optimal combination of Ge contents in a-$Si_{1-x}Ge_x$:H and μc-$Si_{1-y}Ge_y$:H sub-cells was investigated for the a-Si:H/a-$Si_{1-x}Ge_x$:H/μc-Si:H/μc-$Si_{1-y}Ge_y$:H quadruple junction cell structure. Figure 2(a) presents the contour map of the short-circuit current density (J_{sc}) of the quadruple junction TFSCs with x and y variations. The a-Si:H TFSC (x = 0) could not provide adequate current density when used as the secondary sub-cell. Thus, the J_{sc} of the quadruple junction TFSCs is restricted by the secondary sub-cell and remains approximately the same (~8.66 mA·cm^{-2}), as the Ge contents of the μc-$Si_{1-y}Ge_y$:H bottom sub-cells are increased. However, when x is higher than 0.2, the spectral response extension enables the current density of the a-$Si_{1-x}Ge_x$:H sub-cell to match with those of the other sub-cells. Under this circumstance, the J_{sc} values of the quadruple junction TFSCs are mainly determined by those of the μc-$Si_{1-y}Ge_y$:H bottom sub-cells, which increase gradually with the rise of the Ge contents in the μc-$Si_{1-y}Ge_y$:H sub-cells. The highest J_{sc} of ~11.53 mA·cm^{-2} can be obtained by employing the μc-$Si_{0.2}Ge_{0.8}$:H sub-cell. This indicates the capability of this sub-cell to extend the spectral response region.

Figure 2(b) presents the contour map of open-circuit voltage (V_{oc}) of the quadruple junction TFSCs with x and y variations. It is observed from this figure that the V_{oc} decreases with the increase of either x or y, which mainly results from the reduction of the band-gap of the intrinsic layer. The highest V_{oc} in this series is 3.04 V, which is obtained when x = 0 and y = 0.2, while the lowest V_{oc} in this series is 2.48 V, which is obtained when x = 0.6 and y = 0.8. Figure 2(c) presents the contour map of the *FF* values of the quadruple junction TFSCs with x and y variations. An *FF* value of over 84% is obtained when x = 0, which is mainly due to the considerable current difference resulting from the low current density of the secondary sub-cell. When x = 0.1 and the value of y is increased from 0.2 to 0.4, the *FF* value reduces from

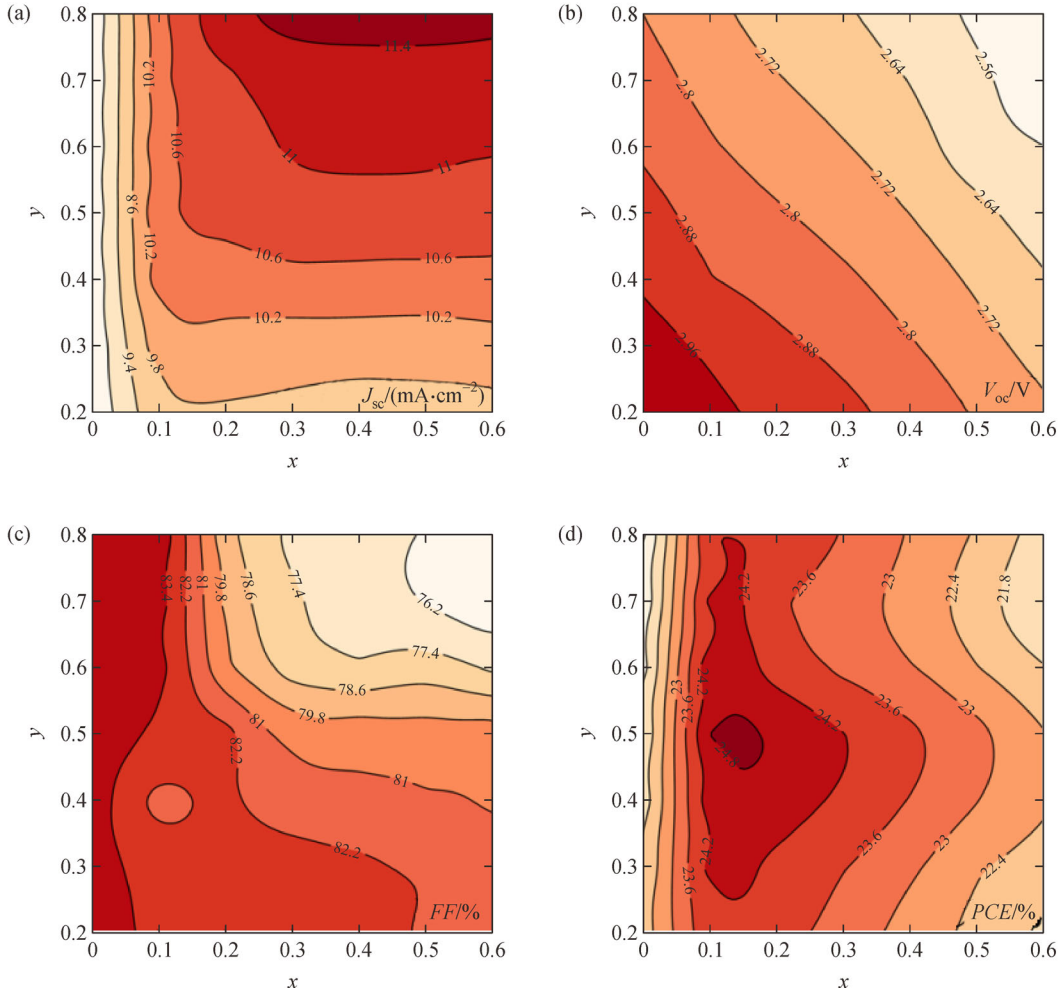

Fig. 2 Contour maps of the performance of quadruple junction TFSCs with varied x and y values. (a) J_{sc}; (b) V_{oc}; (c) fill factor (*FF*); (d) *PCE*.

83.11% to 81.79% due to its reduction in the bottom sub-cell. The *FF* value then rises to 84.35%, as the value of *y* is further increased to 0.8 due to a rise in the current density difference [32]. Moreover, if both *x* and *y* are higher than 0.2, the *FF* value of the quadruple junction TFSCs reduces with an increase in the Ge content of either the a-$Si_{1-x}Ge_x$:H sub-cell or μc-$Si_{1-y}Ge_y$:H sub-cell. This is because, the *FF* values of the a/μc-SiGe:H sub-cells decline with the increase in the Ge contents due to the increment of the intrinsic layer defect density.

The simultaneous variations in V_{oc}, J_{sc}, and *FF* lead to the variation of the *PCE* of the quadruple junction TFSCs. These results are shown in Fig. 2(d). When *x* is less than 0.1, the *PCE* of the quadruple junction TFSCs is very low due to the low J_{sc} value. Once the value of *x* exceeds 0.1, an increase in the J_{sc} and a reduction in the V_{oc} and *FF* values can be induced simultaneously by increasing the Ge content of the bottom sub-cell. The highest *PCE* of 24.80% (V_{oc} = 2.849 V, J_{sc} = 10.47 mA·cm^{-2}, and *FF* = 83.12%) is achieved, when *x* and *y* are 0.1 and 0.5, respectively. Its current density-voltage (*J-V*) and the external quantum efficiency (*EQE*) curves are shown in Fig. 3. The spectral response of the quadruple junction TFSC is effectively extended to 1300 nm by employing the μc-$Si_{0.5}Ge_{0.5}$:H bottom sub-cell. Its *EQE* at 1100 nm is as high as 60% indicating that the spectral energy has been highly utilized. As a result, a J_{sc} of 10.47 mA·cm^{-2} can be obtained by carefully adjusting the thickness of each sub-cell.

The *J-V* and *EQE* curves of each single junction sub-cell in the quadruple junction TFSC with the most optimal performance are shown in Fig. 4(a) and Fig. 4(b), respectively. The parameters of each single sub-cell are shown in Table 1 in detail. The sum of V_{oc} values of the four single junction TFSCs is 2.940 V, while that of the quadruple junction TFSC is 2.849 V. This indicates that there is a some voltage loss in the tunnel recombination junction [33]. As listed in Table 1, the a-Si:H solar cell exhibits a *FF* as high as 88.34%, which mainly comes from the low defect density set in the model and the thin sub-cell thickness [12]. It can be observed that the *PCE* of μc-$Si_{0.5}Ge_{0.5}$:H TFSC is much lower than those of the other three TFSCs. This is because, the μc-$Si_{1-y}Ge_y$:H bottom sub-cell is mainly used to broaden the spectrum absorption region. Therefore, it is expected to possess adequate

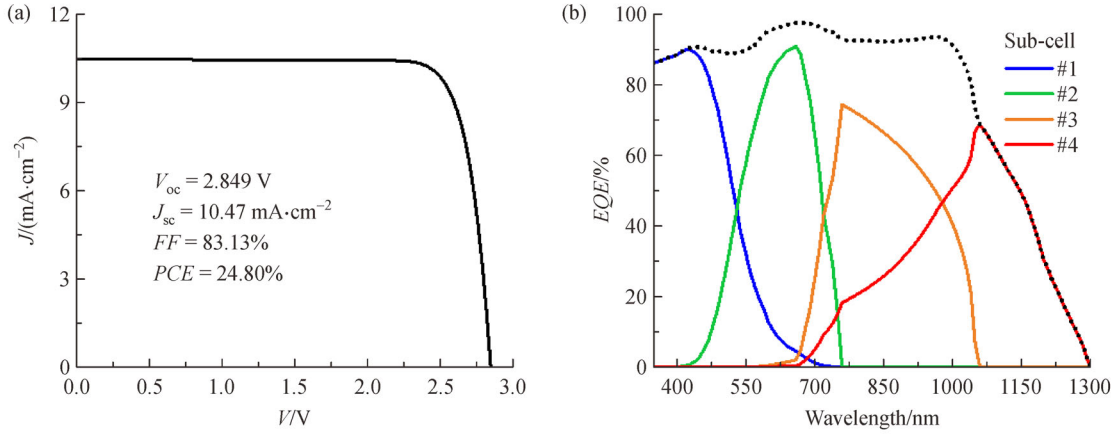

Fig. 3 The most optimal performance of the quadruple junction TFSCs, (a) *J-V* curve; (b) *EQE* curve.

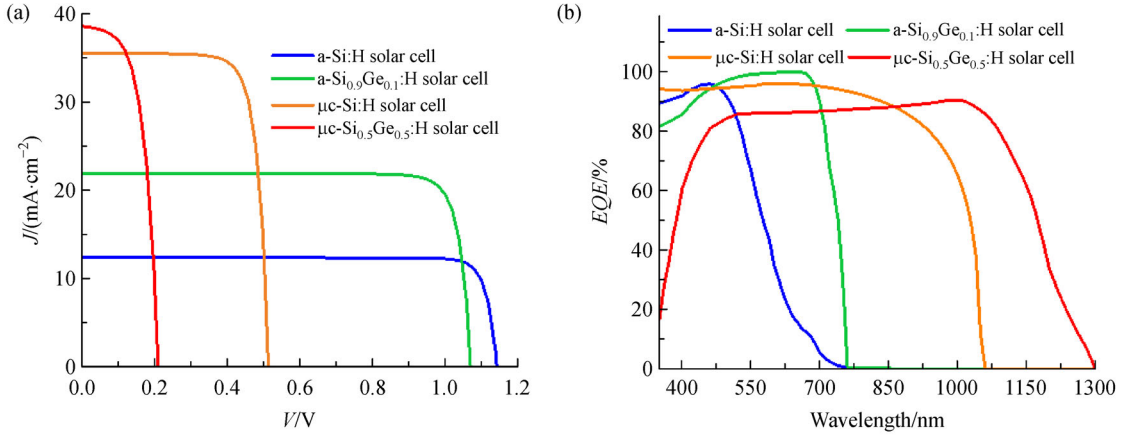

Fig. 4 Performance of each single junction sub-cell. (a) *J-V* curves; (b) *EQE* curves.

Table 1 Parameters of each single sub-cell

Device	Thickness/μm	V_{oc}/V	*FF*/%	J_{sc}/(mA·cm^{-2})	*PCE*/%
a-Si:H TFSC	0.15	1.143	88.34	12.37	12.49
a-$Si_{0.9}Ge_{0.1}$:H TFSC	0.98	1.071	86.11	21.89	20.18
μc-Si:H TFSC	2.20	0.514	78.57	35.49	14.35
μc-$Si_{0.5}Ge_{0.5}$:H TFSC	8.00	0.212	58.36	38.52	4.76

thickness and a low band-gap to absorb as much long-wavelength light as possible. This certainly demonstrated a negative impact on the open-circuit voltage. μc-Si:H is generally used as the p-layer of the μc-$Si_{1-y}Ge_y$:H TFSC, which causes the decline of the short-wave response and *FF* due to the band-gap and lattice mismatch at the p/i interface and leads to a low photoelectric performance [34]. Moreover, an increase in the Ge content in the μc-$Si_{1-y}Ge_y$:H i-layer could result in an increase in the defect state density, which also demonstrates a negative impact on the *FF* and *EQE* response peak of the μc-$Si_{1-y}Ge_y$:H TFSC [29]. However, for quadruple junction TFSCs, we discovered that the disadvantage of the μc-$Si_{1-y}Ge_y$:H sub-cell in terms of low short-wave response could be neglected, because most of the short-wave light is absorbed by the first three sub-cells. As shown in Fig. 3(b), μc-$Si_{1-y}Ge_y$:H sub-cell demonstrates no spectral response until 700 nm. Furthermore, the *FF* of the quadruple junction TFSC could follow the sub-cell with the highest *FF* value using appropriate sub-cell current modulation. The *FF* value of the quadruple junction TFSC is 83.12%, which is much higher than that of μc-$Si_{1-y}Ge_y$:H single junction TFSC (38.52%). Therefore, the effect of the low *FF* of μc-$Si_{1-y}Ge_y$:H sub-cell on the *FF* of the quadruple junction TFSC is also minimal. Consequently, it is observed that the application of μc-$Si_{1-y}Ge_y$:H sub-cell in the quadruple junction TFSC not only broadened the spectral response region but also effectively overcome its own drawbacks, which could improve the photoelectric performance of the quadruple junction TFSC.

The current matching of the quadruple junction TFSC could be obtained by employing an a-$Si_{0.9}Ge_{0.1}$:H sub-cell. However, due to the limitation of the band-gap, only a suitable current of sub-cell with a thickness close to 1 μm could be employed. When the Ge content of a-$Si_{1-x}Ge_x$:H sub-cell was increased to 20%, the same current density could be obtained with the cell thickness as thin as 0.37 μm. Under these circumstances, the TFSC efficiency was estimated at 24.70%, which was only 0.1% less than the maximum *PCE*. Therefore, it is evident that an appropriate amount of reduction of the Ge content in the a-$Si_{1-x}Ge_x$:H sub-cell can facilitate the current matching of the quadruple junction TFSC. Furthermore, according to the study conducted by Yunaz et al., it is notable that x should attain a value of 0.5 to form an optimal a-SiO_z:H/a-$Si_{1-x}Ge_x$:H/μc-$Si_{1-y}Ge_y$:H triple junction TFSC [35]. This is because, the a-$Si_{1-x}Ge_x$:H sub cell in the triple junction TFSC must obtain a much higher current density than the one in the quadruple junction TFSC. This implies that the quadruple junction TFSC structure can reduce not only the thickness of the amorphous sub-cells but also the Ge content of the a-$Si_{1-x}Ge_x$:H sub-cell. Both of these factors are effective in improving the long-term stability of the TFSC. Furthermore, a comparative analysis between the experimental device performance and our simulation result was conducted, which was described in S. 2 of ESM.

The *J-V* and *EQE* curves of the most optimal performance of the a-Si:H/a-$Si_{0.9}Ge_{0.1}$:H/μc-Si:H/μc-$Si_{0.5}Ge_{0.5}$:H quadruple junction TFSCs with varied total thickness values from 8 to 2 μm are shown in Fig. 5(a) and Fig. 5(b), respectively. The parameters of each quadruple junction TFSC are shown in Table 2 in detail. The thickness of each sub-cell is optimized for all the reported total thicknesses and also listed in Table 2. The electrical field over each of the i-layers could be enhanced by reducing the total thickness of the TFSC from 8 to 2 μm. This results in an increase of the FF value from 82.10% to 84.06% due to the improvement of the charge carrier collection efficiency and an increase of the V_{oc} from 2.857 to 2.883 V due to the suppression of carrier recombination [36]. However, the J_{sc} decreases from 10.51 to 8.69 mA·cm^{-2} with the reduction of the quadruple junction TFSC thickness, which attributes to the inefficient light absorption, as shown in Fig. 5(b). Consequently, the *PCE* of the TFSC reduces gradually, as its thickness is decreased. The *PCE* of 24.66% was achieved with the total quadruple junction TFSC of 8 μm thickness, which is slightly lower compared with that of the quadruple junction TFSC with unlimited thickness (24.80%). It can be found that the decrease of the quadruple junction TFSC thickness mainly comes from the change of bottom μc-$Si_{0.5}Ge_{0.5}$:H sub-cell thickness. While the bottom sub-cell determines the infrared absorption of the quadruple junction TFSC. When the μc-$Si_{0.5}Ge_{0.5}$:H sub-cell thickness increases from 0.69 to 1.79 μm, the infrared response of the quadruple junction TFSC is greatly improved, which results in an enhancement of the J_{sc} from 8.69 to 9.82 mA·cm^{-2} and leads to an improved efficiency from 21.07% to 23.38%. However, when the μc-$Si_{0.5}Ge_{0.5}$:H sub-cell is thicker than 2 μm, it became more and more difficult to enhance infrared response by increasing its thickness. Thus, the J_{sc} only increases by 0.69 mA·cm^{-2} as thickness of the μc-$Si_{0.5}Ge_{0.5}$:H cell increases from 1.79 to 4.84 μm, making the device performance only slightly

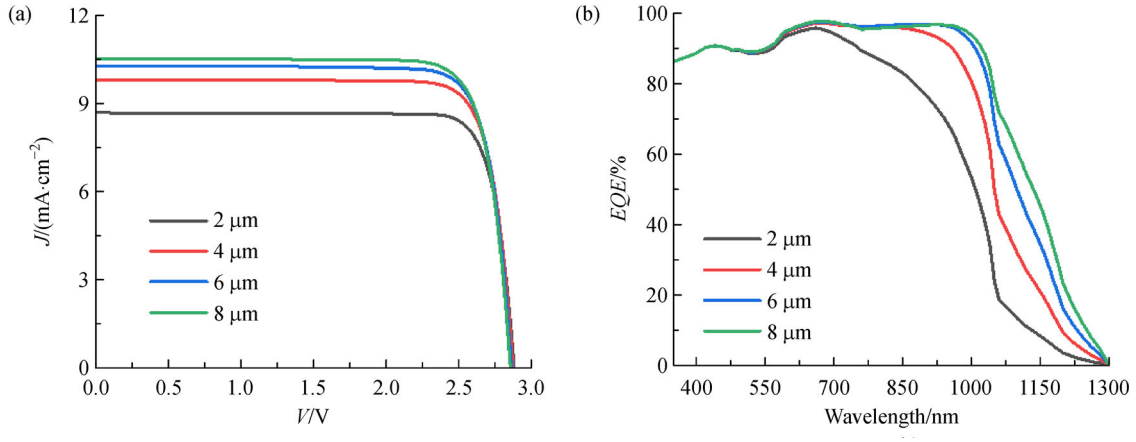

Fig. 5 The a-Si:H/a-$Si_{0.9}Ge_{0.1}$:H/μc-Si:H/μc-$Si_{0.5}Ge_{0.5}$:H quadruple junction TFSCs with varied total thickness values. (a) *J-V* curves; (b) *EQE* curves.

improved. Therefore, although the quadruple junction TFSC with total thickness of 8 μm can achieve the higher efficiency, the design of 4 μm in total thickness is most efficient design in balancing the thickness and *PCE*. Furthermore, it is worth to note that a *PCE* as high as 21.07% can be obtained with the TFSC of 2 μm thickness owing to the improvement of the V_{oc} and *FF* values. The thinner amorphous intrinsic layers could effectively reduce the influence of the Staebler-Wronski effect [37]. However, the simulations do not take the limited carrier diffusion lengths in a-SiGe:H layers into account in the ideal case [38]. In reality, a a-$Si_{1-x}Ge_x$:H solar cell with a thickness thicker than 0.8 μm will have a *FF* much lower than the simulated results due to carrier collection problems. Our results demonstrated that the ultrathin quadruple junction TFSCs with reasonable photoelectric performance could achieve a shorter preparation time as well as a higher long-term stability, which presents a great potential for industrialization.

The optimal performances of the quadruple junction and triple junction TFSCs that employed the μc-$Si_{1-y}Ge_y$:H bottom sub-cell were compared by modifying the total thickness to 4 μm. The cell structures in comparison were a-Si:H/a-$Si_{0.1}Ge_{0.9}$:H/μc-Si:H/μc-$Si_{0.5}Ge_{0.5}$:H and a-Si:H/μc-Si:H/μc-$Si_{0.7}Ge_{0.3}$:H, respectively. Their *J-V* curves and *EQE* curves are plotted in Fig. 6. The triple junction TFSC achieves the highest *PCE* of 20.02% by employing the μc-$Si_{0.7}Ge_{0.3}$:H bottom sub-cell. However, because the band-gap of the first two sub-cells could not be changed, further increase in the Ge content of the bottom sub-cell could no longer compensate for the loss of V_{oc} and *FF* leading to a degradation of the photoelectric performance. In contrast, the quadruple junction TFSC achieves the highest *PCE*, when the Ge content of the μc-$Si_{1-y}Ge_y$:H bottom sub-cell is 50%. Thus, the improved *EQE* responses as 850–1300 nm can be observed in Fig. 6(b). The quadruple junction TFSC achieves a *PCE* of 23.38%, which is 3.36% higher than the highest *PCE* of the triple junction TFSC. Consequently, by employing the μc-$Si_{1-y}Ge_y$:H as the bottom sub-cell, the four sub-cells in the quadruple junction TFSC could provide more reasonable band-gap gradient distribution, which could result in lesser thermalization and non-absorption losses and a higher spectral energy utilization. Furthermore, the results of our study are not only suitable for silicon-based TFSCs, but also can be used as a reference for multi-junction TFSCs composed of other photoactive materials with different band gaps. The technology that changing the band gap through Ge content for a more suitable sub-cell can be referred to as some light-absorbing layer materials such as $Sb_2(S_{1-x}Se_x)_3$ [39] or perovskite [40] that can adjust their band gap by changing the composition.

4 Conclusions

In this work, we designed ultrathin high efficiency solar cells with quadruple junction based on the microcrystalline

Table 2 The optimal performance of a-Si:H/a-$Si_{0.9}Ge_{0.1}$:H/μc-Si:H/μc-$Si_{0.5}Ge_{0.5}$:H quadruple junction TFSCs with varied total thickness values

Thickness/μm	V_{oc}/V	*FF*/%	J_{sc}/(mA·cm^{-2})	*PCE*/%
8 (0.16/1.00/2.00/4.84)	2.857	82.10	10.51	24.66
6 (0.15/0.82/1.83/3.20)	2.866	82.21	10.29	24.23
4 (0.14/0.63/1.44/1.79)	2.876	82.79	9.82	23.38
2 (0.11/0.35/0.85/0.69)	2.883	84.06	8.69	21.07

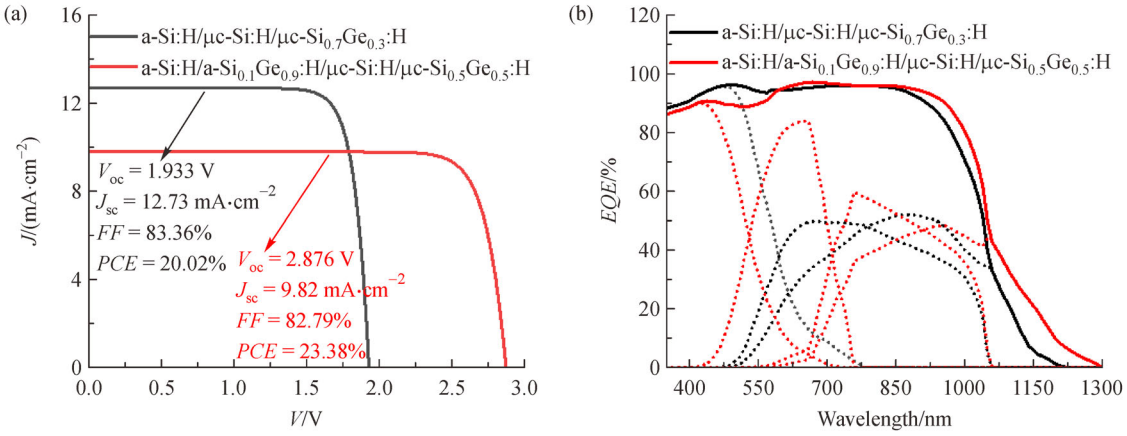

Fig. 6 The most optimal performances of the quadruple junction and triple junction TFSCs with a total thickness of 4 μm. (a) *J-V* curves; (b) *EQE* curves.

Si and Ge alloyed thin films. The highest efficiency 24.80% was achieved with the device structure a-Si:H/a-$Si_{0.9}Ge_{0.1}$:H/μc-Si:H/μc-$Si_{0.5}Ge_{0.5}$:H. Such a record efficiency has been attributed to the perfect gradient distribution of the absorbers in each sub-cells, i.e., 1.78, 1.71, 1.18 and 0.88 eV from top to bottom sub-cells. Further reduction in the thickness of absorber thin films shows satisfying efficiency of 21.07%. Our work may shed light on the experimental guidelines for the alignment of gradient bandgap diagram as well as the design of ultrathin multi-junction solar cells.

Acknowledgements The authors acknowledge Prof. A. Rockett and Dr. Yiming Liu from UIUC and Prof. Fonash of PSU for providing the wxAMPS program. This research was carried out with the support from the National Natural Science Foundation of China (Grant No. 51772049), the Jilin Scientific and Technological Development Program, China (Grant No. 20170520159JH) and the 'Thirteenth Five-Year' Scientific and Technological Research Project of the Education Department of Jilin Province, China (Grant No. JJKH20190705KJ), the project of Jilin Development and Reform Commission (Grant No. 2019C042). The authors also show their gratitude to the National Natural Science Foundation of China (Grant No. 51802116) and the Natural Science Foundation of Shandong Province (No. ZR2019BEM040). Jinbo Pang acknowledges the National Key Research and Development Program of China (Grant No. 2017YFE0102700) from the Ministry of Science and Technology (MOST) of China and the Key Research and Development program of Shandong Province (Major Innovation Project of Science and Technology of Shandong Province) (No. 2018YFJH0503) and the University of Jinan for the Scientific Research Starting Funds.

Electronic Supplementary Material Supplementary material is available in the online version of this article at https://doi.org/10.1007/s11705-019-1906-0 and is accessible for authorized users.

References

1. Wang K, Pang J, Li L, Zhou S, Li Y, Zhang T. Synthesis of hydrophobic carbon nanotubes/reduced graphene oxide composite films by flash light irradiation. Frontiers of Chemical Science and Engineering, 2018, 12(3): 376–382
2. Shu F, Wang M, Pang J, Yu P. A free-standing superhydrophobic film for highly efficient removal of water from turbine oil. Frontiers of Chemical Science and Engineering, 2019, 13(2): 393–399
3. Zhang Y, Xiao J, Lv Q, Wang S. Self-supported transition metal phosphide based electrodes as high-efficient water splitting cathodes. Frontiers of Chemical Science and Engineering, 2018, 12(3): 494–508
4. Zheng H, Picard C, Ravaine S. Nanostructured gold films exhibiting almost complete absorption of light at visible wavelengths. Frontiers of Chemical Science and Engineering, 2018, 12(2): 247–251
5. Uddin M H, Ozalp N, Heylen J, Ophoff C. A new approach for fuel injection into a solar receiver/ reactor: Numerical and experimental investigation. Frontiers of Chemical Science and Engineering, 2018, 12(4): 683–696
6. Isabella O, Vismara R, Linssen D N P, Wang K X, Fan S, Zeman M. Advanced light trapping scheme in decoupled front and rear textured thin-film silicon solar cells. Solar Energy, 2018, 162: 344–356
7. Zhu H, Niu X, Wan M, Mai Y. A study of ZnO:Al thin films reactively sputtered under the control of target voltage for application in Cu (In, Ga) Se_2 thin film solar cells. Vacuum, 2019, 161: 297–305
8. Sun L, Shen H, Huang H, Raza A, Zhao Q, Yang J. Influence of Ge layer location on performance of flexible CZTSSe thin film solar cell. Vacuum, 2019, 165: 186–192
9. Nien Y H, Chen H H, Hsu H H, Kuo P Y, Chou J C, Lai C H, Hu G M, Kuo C H, Ko C C. Enhanced photovoltaic conversion efficiency in dye-sensitized solar cells based on photoanode consisting of TiO_2/GO/Ag nanofibers. Vacuum, 2019, 167: 47–53
10. Xu J, Hu Z, Zhang K, Huang L, Zhang J, Zhu Y. Enhancement in photocurrent through efficient geometrical light trapping in organic photovoltaics. Energy Technology (Weinheim), 2016, 4(2): 314–318
11. Jia X Y, Hu Z Y, Luan S Z, Xu J, Zhang H C, Zhang J, Zhu Y J. Evolution of film morphology in polymer solar cells based on rough electrode substrates. Thin Solid Films, 2016, 616: 690–697

12. Matsui T, Sai H, Bidiville A, Hsu H J, Matsubara K. Progress and limitations of thin-film silicon solar cells. Solar Energy, 2018, 170: 486–498
13. Fang J, Ren Q, Wang F, Wei C, Yan B, Zhao Y, Zhang X. Amorphous silicon/crystal silicon heterojunction double-junction tandem solar cell with open-circuit voltage above 1.5 V and high short-circuit current density. Solar Energy Materials and Solar Cells, 2018, 185: 307–311
14. Trompoukis C, Abass A, Schüttauf J W, Bosserez T, Rongé J, Lauwaert J, Martens J A, Baets R. Porous multi-junction thin-film silicon solar cells for scalable solar water splitting. Solar Energy Materials and Solar Cells, 2018, 182: 196–203
15. Wang X, Guo H, Ma C, Jia X, Li Y, Yuan N, Ding J. Enhancement in the efficiency of Sb_2Se_3 solar cells using a TiO_2-modified SnO_2 buffer layer. Vacuum, 2019, 166: 201–205
16. Meng L, Zhang Y, Wan X, Li C, Zhang X, Wang Y, Ke X, Xiao Z, Ding L, Xia R, et al. Organic and solution-processed tandem solar cells with 17.3% efficiency. Science, 2018, 361(6407): 1094–1098
17. Che X, Li Y, Qu Y, Forrest S R. High fabrication yield organic tandem photovoltaics combining vacuum- and solution-processed subcells with 15% efficiency. Nature Energy, 2018, 3(5): 422–427
18. Sahli F, Werner J, Kamino B A, Brauninger M, Monnard R, Paviet-Salomon B, Barraud L, Ding L, Diaz Leon J J, Sacchetto D, et al. Fully textured monolithic perovskite/silicon tandem solar cells with 25.2% power conversion efficiency. Nature Materials, 2018, 17(9): 820–826
19. Ramírez Quiroz C O, Spyropoulos G D, Salvador M, Roch L M, Berlinghof M, Darío Perea J, Forberich K, Dion-Bertrand L I, Schrenker N J, Classen A, et al. Interface molecular engineering for laminated monolithic perovskite/silicon tandem solar cells with 80.4% fill factor. Advanced Functional Materials, 2019, 29(40): 1901476
20. Li Z, Liang X, Li G, Liu H, Zhang H, Guo J, Chen J, Shen K, San X, Yu W, Schropp R E I, Mai Y. 9.2%-efficient core-shell structured antimony selenide nanorod array solar cells. Nature Communications, 2019, 10(1): 125
21. Deng H, Zeng Y, Ishaq M, Yuan S, Zhang H, Yang X, Hou M, Farooq U, Huang J, Sun K, et al. Quasiepitaxy strategy for efficient full—inorganic Sb_2S_3 solar cells. Advanced Functional Materials, 2019, 29(31): 1901720
22. Cashmore J S, Apolloni M, Braga A, Caglar O, Cervetto V, Fenner Y, Goldbach-Aschemann S, Goury C, Hötzel J E, Iwahashi T, et al. Record 12.34% stabilized conversion efficiency in a large area thin-film silicon tandem (MICROMORPH™) module. Progress in Photovoltaics: Research and Applications, 2015, 23(11): 1441–1447
23. Zhang X, Liu B, Bai L, Wang S, Huang Q, Ni J, Wei C, Zhang D, Sun J, Chen X. Advanced functional materials: Intrinsic and doped silicon oxide. MRS Online Proceedings Library Archive, 2015, 1771: 3–8
24. Liu B, Bai L, Li T, Wei C, Li B, Huang Q, Zhang D, Wang G, Zhao Y, Zhang X. High efficiency and high open-circuit voltage quadruple-junction silicon thin film solar cells for future electronic applications. Energy & Environmental Science, 2017, 10(5): 1134–1141
25. Si F T, Kim D Y, Santbergen R, Tan H R, van Swaaij R A C M M, Smets A H M, Isabella O, Zeman M. Quadruple-junction thin-film silicon-based solar cells with high open-circuit voltage. Applied Physics Letters, 2014, 105(6): 063902
26. Urbain F, Smirnov V, Becker J P, Lambertz A, Rau U, Finger F. Light-induced degradation of adapted quadruple junction thin film silicon solar cells for photoelectrochemical water splitting. Solar Energy Materials and Solar Cells, 2016, 145: 142–147
27. Cao Y, Zhou J, Wang Y, Ni J, Zhang J. Band gap grading in microcrystalline silicon germanium thin film solar cells. Journal of Alloys and Compounds, 2015, 632: 456–459
28. Cao Y, Zhang J, Li C, Li T, Huang Z, Ni J, Hu Z, Geng X, Zhao Y. Hydrogenated microcrystalline silicon germanium as bottom sub-cell absorber for triple junction solar cell. Solar Energy Materials and Solar Cells, 2013, 114: 161–164
29. Cao Y, Liu Y, Zhou J, Wang Y, Ni J, Zhang J. Non-uniform distribution in μc-$Si_{1-x}Ge_x$:H and its influence on thin film and device performance. Solar Energy Materials and Solar Cells, 2016, 151: 1–6
30. Liu Y, Sun Y, Rockett A. A new simulation software of solar cells—wxAMPS. Solar Energy Materials and Solar Cells, 2012, 98: 124–128
31. Yan L, Bai Y, Yang B, Chen N, Tan Z, Hayat T, Alsaedi A. Extending absorption of near-infrared wavelength range for high efficiency CIGS solar cell via adjusting energy band. Current Applied Physics, 2018, 18(4): 484–490
32. Yan B, Yue G, Yang J, Guha S. Correlation of current mismatch and fill factor in amorphous and nanocrystalline silicon based high efficiency multi-junction solar cells. In 2008 33rd IEEE Photovoltaic Specialists Conference. 2008. San Diego, CA, USA, 1–6
33. Bills B, Liao X, Galipeau D W, Fan Q H. Effect of tunnel recombination junction on crossover between the dark and illuminated current-voltage curves of tandem solar cells. IEEE Transactions on Electron Devices, 2012, 59(9): 2327–2330
34. Matsui T, Kondo M, Ogata K, Ozawa T, Isomura M. Influence of alloy composition on carrier transport and solar cell properties of hydrogenated microcrystalline silicon-germanium thin films. Applied Physics Letters, 2006, 89(14): 142115
35. Yunaz I A, Yamada A, Konagai M. Theoretical analysis of amorphous silicon alloy based triple junction solar cells. Japanese Journal of Applied Physics, 2007, 46(47): L1152–L1154
36. Schicho S, Hrunski D, van Aubel R, Gordijn A. High potential of thin (<1 μm) a-Si:H/μc-Si:H tandem solar cells. Progress in Photovoltaics: Research and Applications, 2010, 18(2): 83–89
37. Crandall R S. Defect relaxation in amorphous silicon: Stretched exponentials, the Meyer-Neldel rule, and the Staebler-Wronski effect. Physical Review B: Condensed Matter, 1991, 43(5): 4057–4070
38. Chen J, Zuo L, Zhang Y, Lian X, Fu W, Yan J, Li J, Wu G, Li C Z, Chen H. High-performance thickness insensitive perovskite solar cells with enhanced moisture stability. Advanced Energy Materials, 2018, 8(23): 1800438
39. Yang B, Xue D J, Leng M, Zhong J, Wang L, Song H, Zhou Y, Tang J. Hydrazine solution processed Sb_2S_3, Sb_2Se_3 and $Sb_2(S_{(1-x)}Se_{(x)})_3$ film: Molecular precursor identification, film fabrication and band

gap tuning. Scientific Reports, 2015, 5(1): 10978

40. Yang Z, Yu Z, Wei H, Xiao X, Ni Z, Chen B, Deng Y, Habisreutinger S N, Chen X, Wang K, et al. Enhancing electron diffusion length in narrow-bandgap perovskites for efficient monolithic perovskite tandem solar cells. Nature Communications, 2019, 10(1): 4498